This article has been accepted for publication in a future issue of this journal, but has not been fully edited. Content may change prior to final publication. Citation information: DOI 10.1109/TTE.2020.3033668, IEEE Transactions on Transportation Electrification

Development and Investigation of Novel Axial-Field Dual-Rotor Segmented Switched Reluctance Machine

Wei Sun, *Student Member, IEEE*, Qiang Li, Le Sun, *Member, IEEE*, and Lei Li

***Abstract*—This paper presents a new type of axial-field switched reluctance machine (AFSRM), axial-field dual-rotor segmented switched reluctance machine (ADS-SRM), along with its design methodology. The proposed ADS-SRM is featured by the segmental stator and rotor poles, the auxiliary flux-conductive rings, and the concentrated windings. The yokeless topology reduces the active length of the motor. Besides, the adopted short-end winding layout increases the slot fill factor and the motor's reliability. First, the basic topology of ADS-SRM is introduced along with its operating principle and various stator/rotor pole combinations. The three-phase 12/8 configuration of ADS-SRM is chosen for further analysis. Then, the design methodology considering the fringing and leakage field effects through the magnetic equivalent circuit (MEC) method is developed, and the flowchart detailing the design procedure is presented. Through the comparison with the conventional yokeless and segmented armature (YASA) topology, ADS-SRM exhibits excellent performance at overload conditions. The prototype is designed and fabricated, and the experimental results verify the motor performance.**

***Index Terms*—Axial-field switched reluctance machine (AFSRM), design methodology, magnetic equivalent circuit (MEC), performance comparisons.**

I. Introduction

SWITCHED reluctance machine (SRM) is becoming research focus in recent years due to its unique advantages such as simple and rugged construction, low cost, fault-tolerant operation capability, and high-speed and high-temperature operation adaptabilities [1]-[3]. These features make SRM a good candidate for electric vehicles, electric bicycle, aircraft, railway transport, and other transportation appliances [4]-[9].

Although SRM has the above described features, the absence of the high-energy-density permanent magnets (PMs) in the magnetic structure greatly restricts the power- and torque-density enhancement with respect to the permanent magnet synchronous motor (PMSM), which means that higher current density is in need for the same energy conversion [10]. In the last decades, many efforts have been made in SRM around the world to substitute PMSMs [11]-[15]. It is noted that the high current densities in the coils urgently increase the cooling demands.

To enhance the torque density, many investigations have been implemented on the motor configurations such as the radial- or axial-gap topologies, the multi-gap configurations, and the stator/rotor pole combinations. It has been recognized in literature that the axial-field topologies can have higher torque densities and efficiencies than the radial counterparts as the active air-gap surface area of the former is larger compared with the latter [16], [17]. In addition, the axial-field topologies are suitable for applications with low length-diameter ratio, such as the vehicle wheels [18]. The multi-gap configurations mainly include the Kaman and Torus topologies [17]. The multiple air gaps can significantly increase the utilization of the magnetic flux generated by the excitation coils, thus improving the torque density. To further improve the torque density, SRMs with higher rotor pole number have been introduced [19]-[21].

Rotor-segmented switched reluctance machine (RS-SRM), known as a modular-structure topology, is a group of SRM introduced for the torque-density improvement [22]. However, the adopted multi-tooth winding layout decreases the motor's reliability due to the end-winding overlapping, especially for machines with low length-diameter ratios [23].

Against the drawbacks of the multi-tooth winding layout in RS-SRM, several solutions have been reported. RS-SRMs adopting the auxiliary stator poles and concentrated single-toothed windings are proposed to shorten the end windings [23]. In this configuration, the magnetic flux generated by the excitation coils is mainly circulated by the auxiliary poles, thus shortening the flux paths. However, the auxiliary stator poles inserted in the rotation direction restrains the coil space. Another solution is adopting the toroidal windings, and the double-sided external-rotor configuration is reported to improve the winding utilization [24]. The third solution is adopting the modular motor construction such that the adjacent stator poles can form one motor phase [25]. In this topology, short flux paths without flux reversal is realized. The last solution is adopting the concentrated winding along with the auxiliary magnetic structures forcing the flux paths perpendicular to the revolution direction [26]. In this

Manuscript received XXX, 2020; revised XXX, 2020; accepted XXX, 2020; online XXX, 2020. *(Corresponding author: Wei Sun.)*

The authors are with the School of Automation, Nanjing University of Science and Technology, Nanjing 210094, China (e-mail: sunwei_njust@foxmail.com; chnliqiang@njust.edu.cn; sunle@njust.edu.cn; lileinjust@njust.edu.cn).

2332-7782 (c) 2020 IEEE. Personal use is permitted, but republication/redistribution requires IEEE permission. See http://www.ieee.org/publications_standards/publications/rights/index.html for more information.
Authorized licensed use limited to: Auckland University of Technology. Downloaded on December 19,2020 at 19:54:57 UTC from IEEE Xplore. Restrictions apply.

This article has been accepted for publication in a future issue of this journal, but has not been fully edited. Content may change prior to final publication. Citation information: DOI 10.1109/TTE.2020.3033668, IEEE Transactions on Transportation Electrification

configuration, the auxiliary magnetic structures do not conflict with the coil space. However, the active axial length can be further reduced through the configuration of double-sided external rotors with single internal stator [27].

In this paper, a novel axial-field dual-rotor segmented switched reluctance machine (ADS-SRM) is presented. The configuration of double-sided external rotors with single internal stator results in the removal of the stator yoke, thus reducing the motor size, while there is no degradation in the motor's torque-production capability. Furthermore, the adopted ring-shape auxiliary magnetic structures, which shorten the main flux generated by the excitation coils, ensure the magnetic isolation among adjacent phases.

This paper is organized as follows: Descriptions of the basic motor topology of ADS-SRM, along with the optimization of the stator/rotor pole combination, are given in Section II. The design methodology for the motor is presented in Section III. The comparisons of the performance of ADS-SRM with that of the yokeless and segmented armature AFSRM (YASA-AFSRM) are detailed in Section IV. A prototype is fabricated and the construction details are explained in Section V. The experimental verification is in Section VI, followed by the conclusions in Section VII.

II. ADS-SRM Topology and Principle

A. Basic Topology Details

The basic topology of the proposed ADS-SRM is shown in Fig. 1(a). It consists of single inner stator and double-sided external rotors. The stator contains the excitation pole and the outer and inner flux-conductive rings. The rotor is composed of the rotor segments in pairs, which are installed at the opposite sides. The main flux paths in the basic topology in the 3D and 2D cross-sectional views are shown in Figs. 1(b) and 1(c). As depicted in Figs. 1(b) and 1(c), the flux is generated by the coil wrapped around the excitation pole, and splits into two branches after flowing into the rotor segment. One branch consists of the outer flux-conductive ring and the outer air gaps, and the other consists of the inner flux-conductive ring and the inner air gaps. The proposed ADS-SRM has the following features.

1) Balanced axial magnetic force when the rotor segments at the opposite rotor sides are in alignment.

2) Concentrated winding layout featured with no end-winding overlapping and shorter coil end is adopted.

3) The flux paths are mainly circulated by the outer and inner flux-conductive rings. The independent and short flux paths contribute to the modular feature.

4) The cancellation of the stator yoke shortens the axial length of the machine, thus increasing the torque density.

5) All the rotor segments are embedded in the rotor brackets made of high-mechanical-strength nonmagnetic materials, thus suppressing the vibration.

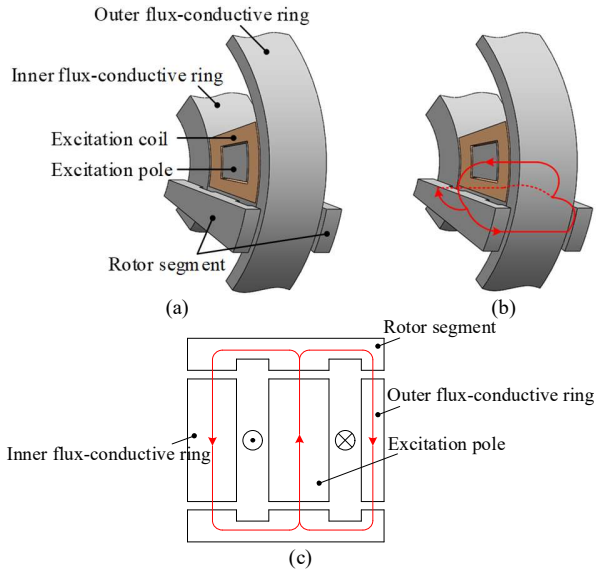

Fig. 1. Basic topology and principle of ADS-SRM. (a) Basic topology. Main flux paths in (b) 3D and (c) 2D cross-sectional views.

B. Various Stator/Rotor Pole Combinations

In Fig. 1, only one excitation pole and a pair of rotor segments are presented. The rotor segments of the basic topology can only rotate for a certain angle until they are aligned with the excitation pole. For continuous operation, specific stator/rotor pole combinations are required. For ADS-SRM, the main flux is generated by a single excitation pole as shown in Fig. 1. Hence, the stator pole number Z_s can be arbitrary multiples of the phase number m. The common combinations of the stator/rotor pole numbers Z_s/Z_r are $mx/(m\pm1)x$. Here, the multiple x should be a positive integer greater than 1 to ensure the balanced operation [28]. Both m and x can affect the motor performance [29].

In order to evaluate the effect of m and x fairly, motors in various stator/rotor pole combinations are designed at the same ratings, i.e. 1 kW at 2000 r/min. In addition, all motors have the same overall dimensions, i.e. the same outer dimension and total length. Considering one ADS-SRM phase, the converted energy can be calculated using (1) based on the flux linkage-current diagrams, which are obtained by 3D finite-element method (FEM). Here, it is assumed that the flux linkage is constant near unaligned or aligned rotor positions. The average torque can be obtained by (2).

$$W_{conv}(i)=\int_0^i \psi_a(i)\,\mathrm{d}i-\int_0^i \psi_u(i)\,\mathrm{d}i \tag{1}$$

$$T_{avg}(i)=\frac{W_{conv}(i)}{2\pi/mZ_r} \tag{2}$$

where Ψ_u and Ψ_a are the flux linkages at unaligned and aligned rotor positions, respectively.

The effects of m and x on the torque production capabilities in terms of phase current are shown in Fig. 2. It is observed that,

1) Slightly higher torque output is exhibited at low current levels when the rotor pole number is larger than the stator pole number, e.g. the average torque of the four-phase 16/12 configuration is about 91% that of the four-phase 16/20 configuration at 4 A. However, significantly higher torque

2332-7782 (c) 2020 IEEE. Personal use is permitted, but republication/redistribution requires IEEE permission. See http://www.ieee.org/publications_standards/publications/rights/index.html for more information.
Authorized licensed use limited to: Auckland University of Technology. Downloaded on December 19,2020 at 19:54:57 UTC from IEEE Xplore. Restrictions apply.

This article has been accepted for publication in a future issue of this journal, but has not been fully edited. Content may change prior to final publication. Citation information: DOI 10.1109/TTE.2020.3033668, IEEE Transactions on Transportation Electrification

output is exhibited at high current levels when the rotor pole number is smaller than the stator pole number, e.g. the average torque of the four-phase 16/12 configuration is about 1.2 times that of the four-phase 16/20 configuration at 20 A.

2) With the increase of *m*, the torque output increases at low current levels, while it decreases at high current levels when the rotor pole number is smaller than the stator pole number. For example, the average torques for the three-phase 12/8, four-phase 16/12, and five-phase 20/16 configurations at 4 A are 1.49 N·m, 1.67 N·m, and 2 N·m, respectively, while they are 21.7 N·m, 19.4 N·m, and 18.7 N·m respectively at 20 A.

3) The torque outputs for various *x* at low current levels are almost identical, while the torque output increases with the increase of *x* at high current levels.

4) When $x \leqslant 4$, the torque output increases significantly with the increase of *x*. After that, the torque outputs are almost the same.

On the other hand, both higher *m* and *x* can lead to higher commutation frequency, thus producing higher switching loss. Moreover, higher *m* can increase the cost of the converter.

In order to have a compromise among the torque production capability, the commutation frequency, and the converter cost, the three-phase 12/8 configuration is a good choice.

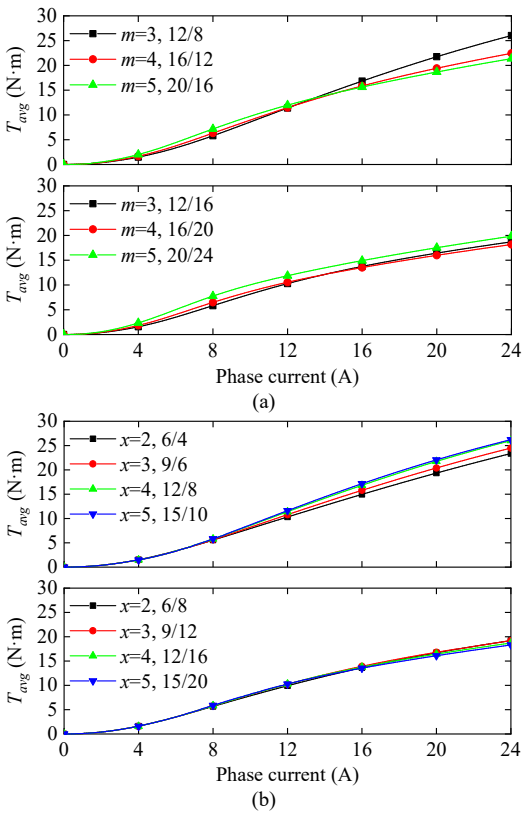

Fig. 2. (a) Effect of *m* on the torque production capability under various current levels when *x*=4. (b) Effect of *x* on the torque production capability under various current levels when *m*=3.

C. Three-Phase 12/8 ADS-SRM

Fig. 3(a) shows the discussed three-phase 12/8 ADS-SRM. It consists of three phases, each with four excitation poles. The excitation poles belonging to each phase are located 90°mech apart from each other, and the coils wrapped around them are connected in series with the same winding polarity. All the excitation poles are magnetically isolated from each other. The rotor consists of eight rotor segments at each rotor side, and all of them are separated from each other. Figs. 3(b) and 3(c) show the magnetic field distributions in the three-phase 12/8 ADS-SRM with typical geometric dimensions at unaligned and aligned rotor positions, respectively. The flux linkage characteristics at unaligned and aligned rotor positions are depicted in Fig. 4. It is noted that high saturation of the iron core occurs at aligned rotor position at high current levels.

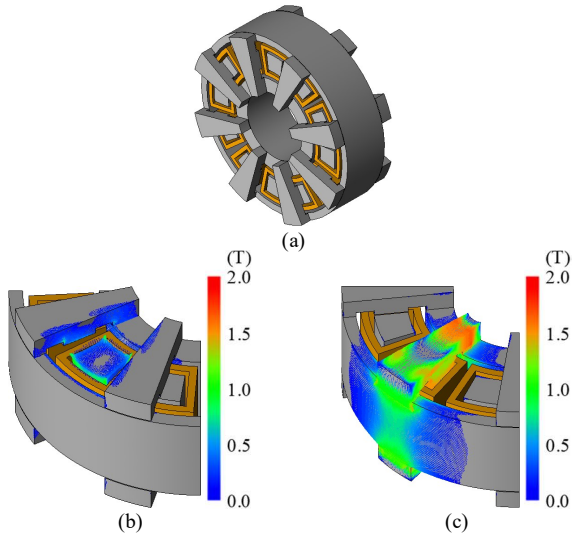

Fig. 3. Discussed three-phase 12/8 ADS-SRM. (a) 3D view of the motor geometry. (b) Magnetic field distribution at unaligned rotor position. (c) Magnetic field distribution at aligned rotor position.

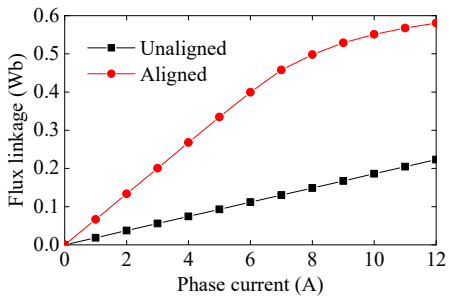

Fig. 4. Flux linkage characteristics at unaligned and aligned rotor positions.

III. Design Methodology

The basic topology and main dimensions of the three-phase 12/8 ADS-SRM are shown in Fig. 5. Fig. 5(b) is the cross section A-A in Fig. 5(a). Figs. 5(c) and 5(d) are respectively the cross sections B-B and C-C in Fig. 5(b). It is noted that there exist three air gaps for each rotor segment at each side. This should be considered in the magnetic equivalent circuits (MECs). Besides, unlike the general SRMs, each excitation pole of ADS-SRM is close to three rectangular slots, which should be considered in the winding design.

2332-7782 (c) 2020 IEEE. Personal use is permitted, but republication/redistribution requires IEEE permission. See http://www.ieee.org/publications_standards/publications/rights/index.html for more information.
Authorized licensed use limited to: Auckland University of Technology. Downloaded on December 19,2020 at 19:54:57 UTC from IEEE Xplore. Restrictions apply.

This article has been accepted for publication in a future issue of this journal, but has not been fully edited. Content may change prior to final publication. Citation information: DOI 10.1109/TTE.2020.3033668, IEEE Transactions on Transportation Electrification

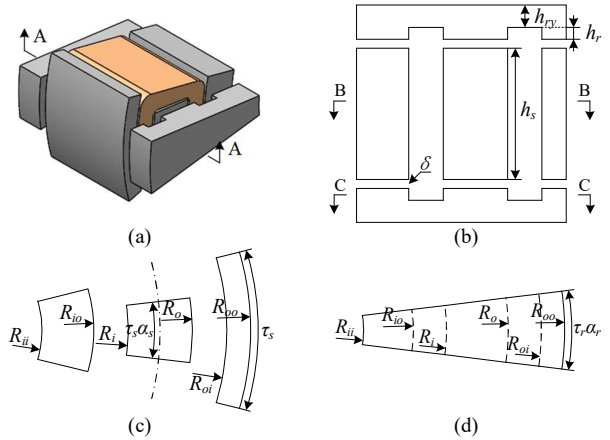

Fig. 5. Basic topology and main dimensions of ADS-SRM. (a) Basic topology. (b) Cross section A-A. (c) Cross section B-B. (d) Cross section C-C.

A. Flux Patterns and Magnetic Equivalent Circuits

Fig. 6 describes the flux patterns in the air region of ADS-SRM. The air-gap flux paths on the circumferential and radial cross sections at unaligned rotor position are shown in Figs. 6(a) and 6(b), respectively, and those on the circumferential and radial cross sections at aligned rotor position are shown in Figs. 6(c) and 6(d), respectively. The corresponding MECs are given in Fig. 7.

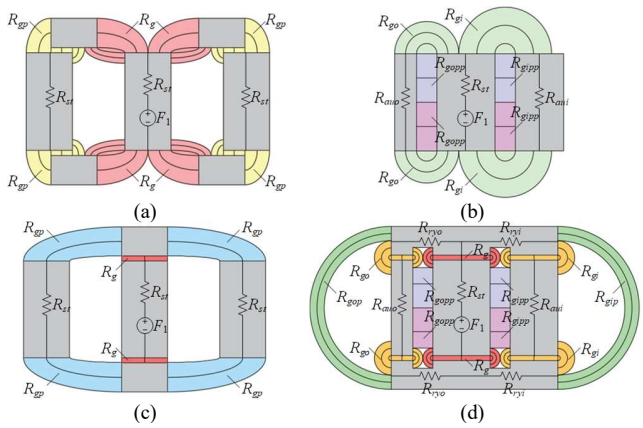

Fig. 6. Flux patterns in the air region on the (a) circumferential and (b) radial cross sections at unaligned rotor position, and those on the (c) circumferential and (d) radial cross sections at aligned rotor position.

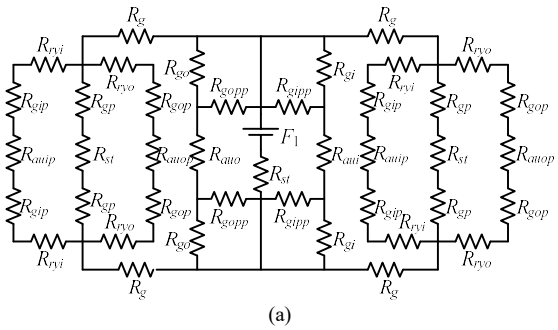

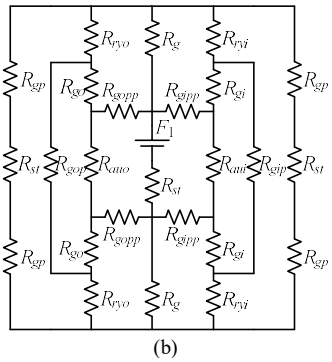

Fig. 7. MECs of ADS-SRM at (a) unaligned and (b) aligned rotor positions.

The magnetomotive force (MMF) of the coils wrapped around each excitation pole is

$$F_1 = \frac{N_{ph} i}{4} \tag{3}$$

where N_{ph} is the number of winding turns in series per phase; i is the phase current.

Assuming that the permeance of iron core is much greater than that of vacuum, the reluctance of iron core is thus neglected. At unaligned rotor position, the total reluctance (R_u) is

$$R_u = \frac{2}{\frac{1}{R_{gi}} + \frac{1}{R_{gipp}} + \frac{1}{R_{go}} + \frac{1}{R_{gopp}} + \frac{2\left(R_{gop}R_{gp} + R_{gip}R_{gop} + R_{gip}R_{gp}\right)}{R_{gip}R_{gop}R_{gp} + R_g R_{gop}R_{gp} + R_g R_{gip}R_{gop} + R_g R_{gip}R_{gp}}} \tag{4}$$

The phase inductance at unaligned rotor position (L_u) is

$$L_u = \frac{N_{ph}^2}{8}\left(\frac{1}{R_{gi}} + \frac{1}{R_{gipp}} + \frac{1}{R_{go}} + \frac{1}{R_{gopp}} + \frac{2\left(R_{gop}R_{gp} + R_{gip}R_{gop} + R_{gip}R_{gp}\right)}{R_{gip}R_{gop}R_{gp} + R_g R_{gop}R_{gp} + R_g R_{gip}R_{gop} + R_g R_{gip}R_{gp}}\right) \tag{5}$$

At aligned rotor position, the total reluctance (R_a) and phase inductance (L_a) can be obtained through the following process.

$$A = R_{gp} // \frac{R_{gop}}{2} // R_{go} \tag{6}$$

$$B = R_{gp} // \frac{R_{gip}}{2} // R_{gi} \tag{7}$$

$$C = \frac{AR_g + AB + BR_g}{B} \tag{8}$$

$$D = \frac{AR_g + AB + BR_g}{R_g} \tag{9}$$

$$E = \frac{AR_g + AB + BR_g}{A} \tag{10}$$

$$F = C // R_{gopp} \tag{11}$$

$$G = E // R_{gipp} \tag{12}$$

$$X = \frac{FG}{D + F + G} \tag{13}$$

$$Y = \frac{DF}{D + F + G} \tag{14}$$

$$Z = \frac{DG}{D + F + G} \tag{15}$$

$$R_a = 2X + 2Y // 2Z \tag{16}$$

$$L_a = \frac{N_{ph}^2}{4R_a} \tag{17}$$

The phase inductance coefficient (K_u) is defined by (18). The

2332-7782 (c) 2020 IEEE. Personal use is permitted, but republication/redistribution requires IEEE permission. See http://www.ieee.org/publications_standards/publications/rights/index.html for more information.
Authorized licensed use limited to: Auckland University of Technology. Downloaded on December 19,2020 at 19:54:57 UTC from IEEE Xplore. Restrictions apply.

This article has been accepted for publication in a future issue of this journal, but has not been fully edited. Content may change prior to final publication. Citation information: DOI 10.1109/TTE.2020.3033668, IEEE Transactions on Transportation Electrification

empirical value of K_u is between 0.65 and 0.75 [1].

$$K_u = 1 - \frac{L_u}{L_a} \tag{18}$$

As shown in Fig. 6(d), the reluctance of the flux paths in the air region between the excitation pole and the rotor segment considering the fringing field consists of three components (R_{g1}, R_{g2}, and R_{g3}). R_{g1} is the air-gap reluctance of the overlap region between the excitation pole top surface and the rotor segment, and R_{g2} and R_{g3} are the reluctances of the fringing field at the outer and inner sides of the excitation pole tip, respectively. The fringing field coefficient (k_f) is defined as

$$k_f = \frac{R_{g1} // R_{g2} // R_{g3}}{R_{g1}}. \tag{19}$$

In addition to the fringing field, there also exists flux leakage between the side surfaces of the excitation pole and the flux-conductive rings as shown in Fig. 6(d). The leakage field between the adjacent excitation poles can be neglected due to large air gap. The ratio of the total reluctance considering the leakage field effect to that not considering the leakage effect is defined as the leakage field coefficient (k_l) in (20).

$$k_l = \frac{R_a}{R_a \big|_{R_{gp} \,\&\, R_{gopp} \,\&\, R_{gipp} = \infty}} \tag{20}$$

The above derived phase inductance coefficient (K_u), fringing field coefficient (k_f), and leakage field coefficient (k_l) are the three calibration factors in the iterative process for the motor design. Table I summarizes the comparisons of the analytical results with those from 3D finite-element analysis (FEA) when the saturation does not occur for ADS-SRM with typical geometric dimensions. The accuracy of the developed MEC model is thus validated. Fig. 8 shows the variations of the unaligned and aligned phase inductances along with the three coefficients with the phase current by 3D FEM. It is indicated that L_a decreases when the phase current is higher than 6 A due to the saturation, while L_u is independent of the phase current. This leads to the decreased K_u when the phase current is higher than 6 A. On the contrary, k_f and k_l are almost independent of the saturation.

TABLE I
VERIFICATION OF ANALYTICAL RESULTS NEGLECTING SATURATION FOR ADS-SRM WITH TYPICAL GEOMETRIC DIMENSIONS

Parameter	MEC	3D FEM	Discrepancy (%)
L_u (mH)	18.1	17.7	2.26
L_a (mH)	63.1	66.4	-4.97
K_u	0.713	0.733	-2.73
k_f	0.935	0.921	1.52
k_l	0.824	0.846	-2.6

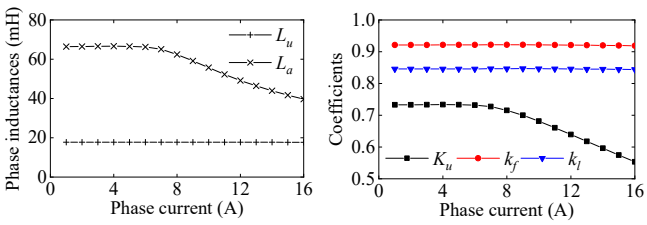

Fig. 8. Variations of (a) phase inductances and (b) three coefficients with phase current by 3D FEM.

B. Output Equation

In order to obtain the geometric parameters of ADS-SRM, it is necessary to derive its output equation first. A design procedure for axial-field SRM is proposed in [30], but the output equation is only suitable for specific motor topology. The design procedure presented in [26] can be applied to the discussed ADS-SRM due to the similar motor topology. However, some modifications should be made in the design procedure since the MECs of the two machines are not exactly identical.

Assuming the ideal square-waveform phase current and linear phase inductance, the average torque can be expressed as (21) based on the virtual work method [31].

$$T_{avg} = \frac{1}{2} I_{ph}^2 \frac{L_a - L_u}{2\pi / mZ_r} \tag{21}$$

where I_{ph} is the amplitude of the flat-top phase current during the phase excitation period.

The root-mean-square (RMS) value of phase current (I_{RMS}) and the change of phase inductance ΔL are given in (22) and (23), respectively [1], [26].

$$I_{RMS} = \sqrt{\frac{1}{T}\int_0^T I_{ph}^2 \,\mathrm{d}t} = \frac{I_{ph}}{\sqrt{m}} = k_i i_m \tag{22}$$

$$\Delta L = L_a - L_u = L_a\left(1 - \frac{L_u}{L_a}\right) = L_a K_u \tag{23}$$

where T is the period of phase conduction; i_m is the peak value of phase current; k_i is the phase current coefficient, which is the ratio of I_{RMS} to i_m.

The phase inductance at aligned rotor position (L_a) can be obtained based on the MEC model of the motor. As shown in Figs. 6 and 7, the MEC at aligned rotor position is too complex due to the fringing and leakage field, complicating the computation at the initial design stage. Since the main flux paths in ADS-SRM are independent, the simplified main flux circuit of single excitation pole at aligned rotor position is shown in Fig. 9. In Fig. 9, R_g, R_{go}, and R_{gi} are the reluctances of the air gaps at the excitation pole, the outer and inner flux-conductive rings, respectively, not considering the fringing and leakage field.

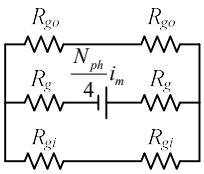

Fig. 9. Simplified MEC of single excitation pole at aligned rotor position.

Based on the simplified flux circuit, L_a can be obtained as (24). Besides, the relationship expressed by (25) can be obtained.

$$L_a = \frac{4}{c} \cdot \frac{1}{c} \cdot \frac{\left(\frac{cN_{ph}}{4}\right)^2}{kk_f k_l \left(2R_g + 2R_{go} // 2R_{gi}\right)} = \frac{N_{ph}^2 \mu_0 \pi D_{av} \alpha_s l_{ef}}{16 k k_f k_l \delta Z_s} \tag{24}$$

$$\frac{cN_{ph}}{4}\frac{i_m}{c} = \frac{N_{ph}}{4} i_m = \frac{4kk_f k_l B_\delta \delta}{\mu_0} \tag{25}$$

where k_f and k_l are introduced based on the derivations in

2332-7782 (c) 2020 IEEE. Personal use is permitted, but republication/redistribution requires IEEE permission. See http://www.ieee.org/publications_standards/publications/rights/index.html for more information.
Authorized licensed use limited to: Auckland University of Technology. Downloaded on December 19,2020 at 19:54:57 UTC from IEEE Xplore. Restrictions apply.

This article has been accepted for publication in a future issue of this journal, but has not been fully edited. Content may change prior to final publication. Citation information: DOI 10.1109/TTE.2020.3033668, IEEE Transactions on Transportation Electrification

Section III-A; k is the coefficient considering the saturation, and k=1.05 in this design; c is the branch number of each phase winding; $D_{av}=R_o+R_i$ and $l_{ef}=R_o-R_i$, are the average armature diameter and the radial thickness of the excitation pole, respectively; $\mu_0=4\pi\times10^{-7}$, is the magnetic permeability of vacuum; B_δ is the average flux density at i_m, and B_δ=1.8 T in this design [32].

The relationship between the output power (P_2) and the average torque (T_{avg}) can be expressed as

$$P_2 = T_{avg}\frac{\pi n}{30} \tag{26}$$

where n is the base speed.

Based on the above equations, the output equation for ADS-SRM can be derived and is expressed as

$$P_2 = \frac{2K_u m^2 \pi \alpha_s Z_r n B_\delta^2 k \delta k_i^2 k_f k_l D_{av} l_{ef}}{15\mu_0 Z_s}. \tag{27}$$

The yoke height of the rotor segment (h_{ry}) is empirically in the range of (0.5-1)l_{ef}. The thicknesses of the outer and inner flux-conductive rings ($l_{efo}=R_{oo}-R_{oi}$ and $l_{efi}=R_{io}-R_{ii}$), the average diameters of the outer and inner flux-conductive rings ($D_{avo}=R_{oo}+R_{oi}$ and $D_{avi}=R_{io}+R_{ii}$), and the slot height (h_s) are determined by the winding design.

C. Winding Design

By referencing [26], the phase turn number (N_{ph}) and the strand number of the coil (N_p) are obtained by (28) and (29), respectively.

$$N_{ph} = \frac{16\sqrt{2}kk_i k_m k_d B_\delta \delta m V_{DC}\eta}{\mu_0 P_2} \tag{28}$$

$$N_p = \frac{\sqrt{k_d} I_{ph}}{cJ\dfrac{\pi d_{coil}^2}{4}} = \frac{4\sqrt{k_d} I_{ph}}{c\pi J d_{coil}^2} \tag{29}$$

where d_{coil} is the diameter of the enameled wire; J is 5.5 A/mm^2 in this design as the natural cooling method is employed.

As shown in Fig. 3, each excitation pole of ADS-SRM is adjacent to three different rectangular slots. The slot height (h_s), i.e. the axial length of the stator, can be obtained based on the three computed slot heights as expressed by (30).

$$h_s = \max(h_{so}, h_{si}, h_{sm}) \tag{30}$$

where h_{so}, h_{si}, and h_{sm} are the computed slot heights of the slots at the outer side, inner side, and circumferential side of the excitation pole, respectively. The three slot heights are expressed as

$$\begin{cases} h_{so} = \dfrac{\pi d_{coil}^2 N_p N_{ph} m}{2Z_s k_{slo}\left(D_{avo} - D_{av} - l_{ef} - l_{efo}\right)} \\ h_{si} = \dfrac{\pi d_{coil}^2 N_p N_{ph} m}{2Z_s k_{sli}\left(D_{av} - D_{avi} - l_{ef} - l_{efi}\right)} \\ h_{sm} = \dfrac{\pi d_{coil}^2 N_p N_{ph} m}{2k_{slm}\pi\left(D_{av} - l_{ef}\right)\left(1-\alpha_s\right)} \end{cases}. \tag{31}$$

In (31), k_{slo}, k_{sli}, and k_{slm} are the slot-fill factors of the coils at the outer side, inner side, and circumferential side of the excitation pole, respectively.

In the design procedure, D_{av}, D_{avo}, and D_{avi} are the three variables adjusted iteratively under the constraints of

$$\begin{cases} k_{slo} = k_{sli} = 0.4 \\ k_{slm} = 0.5 \\ R_{oo} \le 100\text{mm} \\ R_{ii} \ge 15\text{mm} \end{cases}. \tag{32}$$

The flowchart of design methodology is shown in Fig. 10. As shown in Fig. 10, the flowchart consists of four steps. At the preliminary step, the specifications of ADS-SRM are introduced, including the rated parameters, the constraints, and the configurations. The rated parameters are given in Table II. The constraints are given in (32). The configurations include m, (Z_s and Z_r), (α_s and α_r), and the winding layout. In this motor, the winding polarities of all coils are the same, eliminating the flux reversals in the iron core. The approximate dimensions of ADS-SRM can be obtained through the output equation and the winding design when K_u, k_f, and k_l are empirically evaluated. The second step is to check whether the constraints of the motor are satisfied. Fine adjustment of the motor geometry is necessary until the constraints are met. After then, iterative computation is implemented for the accuracy of the three calibration factors (K_u, k_f, and k_l) which are involved in the algebraic computation. The last step is to ensure the motor performance requirement. The main geometric data of ADS-SRM at the initial design stage are provided in Table III.

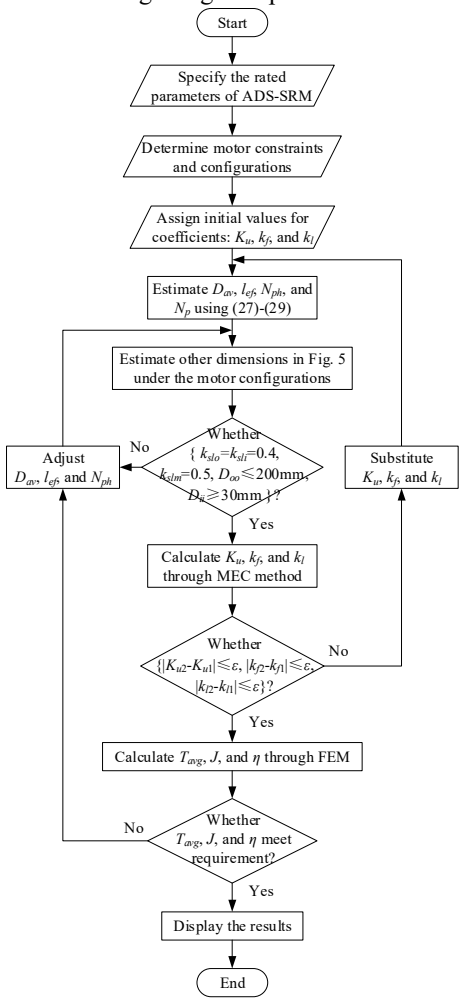

Fig. 10. Flowchart of ADS-SRM design.

2332-7782 (c) 2020 IEEE. Personal use is permitted, but republication/redistribution requires IEEE permission. See http://www.ieee.org/publications_standards/publications/rights/index.html for more information.
Authorized licensed use limited to: Auckland University of Technology. Downloaded on December 19,2020 at 19:54:57 UTC from IEEE Xplore. Restrictions apply.

This article has been accepted for publication in a future issue of this journal, but has not been fully edited. Content may change prior to final publication. Citation information: DOI 10.1109/TTE.2020.3033668, IEEE Transactions on Transportation Electrification

TABLE II
DESIGN SPECIFICATIONS OF ADS-SRM

Parameter	Symbol	Value
Output power (kW)	P_2	1
DC-link voltage (V)	V_{DC}	288
Current density (A/mm^2)	J	5.5
Efficiency (%)	η	75
Base speed (r/min)	n	2000
Average torque (N·m)	T_{avg}	4.77

TABLE III
MAIN GEOMETRIC DATA AT INITIAL DESIGN STAGE

Parameter	Value	Parameter	Value
Z_s/Z_r	12/8	N_{ph}	225×4
R_{ii} (mm)	37.141	R_{io} (mm)	52.762
R_i (mm)	63.084	R_o (mm)	82.391
R_{oi} (mm)	92.713	R_{oo} (mm)	100
h_s (mm)	50.752	δ (mm)	0.5
h_{ry} (mm)	9	h_r (mm)	3
$\tau_s\alpha_s$ (°)	15	$\tau_r\alpha_r$ (°)	15
N_p	1	d_{coil} (mm)	1.05
Grade	50DW470	k_{sl}	0.4, 0.5

D. Effect of Main Geometric Parameters

In the previous section, MEC method is incorporated into the design procedure of ADS-SRM, and some geometric parameters such as h_r, h_{ry}, α_s and α_r are determined empirically. These parameters have been verified as influential optimization variables through the sensitivity analysis [33], [34]. Hence, the influences of these parameters on the motor performance are investigated by 3D FEM for optimization. The effects of rotor slot height (h_r) and rotor yoke height (h_{ry}) at the phase excitation of 8 A, i.e. the current density of 5 A/mm^2, are shown in Figs. 11 and 12, respectively. The effect on the copper loss is not considered since the stator dimensions and MMF remain unchanged.

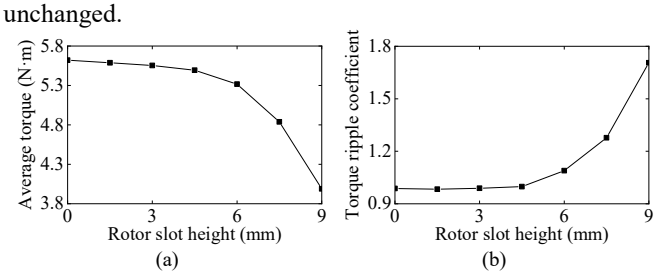

Fig. 11. Effect of rotor slot height on (a) average torque and (b) torque ripple coefficient.

As shown in Fig. 11(a), with the increase of rotor slot height, the average torque decreases monotonously, while the torque ripple increases. The output capability of the motor is maximized without the rotor slot. This is due to the increased degree of saturation at the rotor segment yoke when the rotor slot height increases.

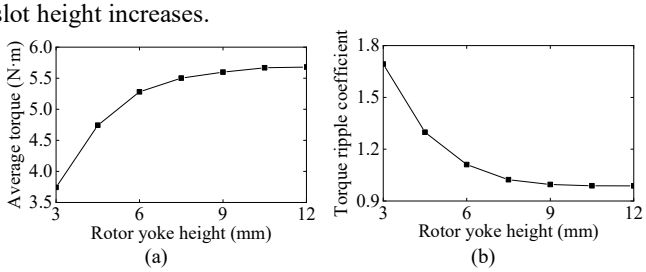

Fig. 12. Effect of rotor yoke height on (a) average torque and (b) torque ripple coefficient.

Fig. 12 indicates that when the rotor yoke height is reduced from 12 mm to 9 mm, that is, by 25%, the average torque is reduced by only 1.4% and the torque ripple coefficient is increased by only 0.8%. Therefore, 25% of the iron core in the rotor segment is extra, and the removal of this extra part can reduce the motor size.

The effects of the stator and rotor pole arc angles ($\tau_s\alpha_s$ and $\tau_r\alpha_r$) in normalization at the phase excitation of 8 A are shown in Fig. 13. Here, the motor performances when h_r=0 mm and h_{ry}=9 mm are selected as the base values.

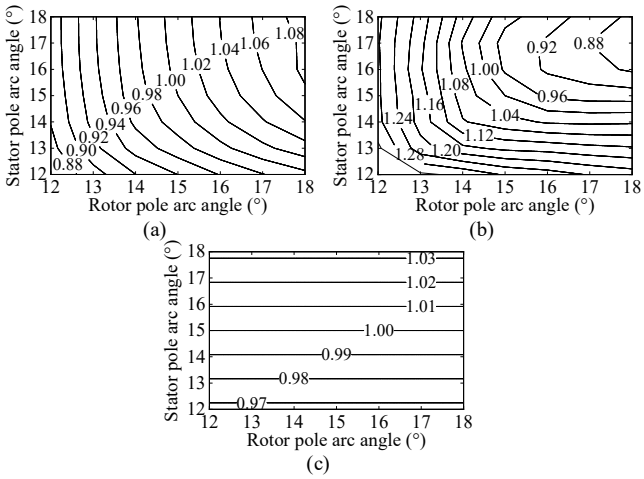

Fig. 13. Effect of stator and rotor pole arc angles on (a) P.u. of average torque, (b) P.u. of torque ripple coefficient, and (c) P.u. of copper loss.

As shown in Fig. 13, both the stator and rotor pole arc angles can have significant effect on the motor performance. To make a tradeoff between the average torque, the torque ripple, and the copper loss, an objective function is defined as (33), and is shown in Fig. 14.

$$F(x,y)=\frac{T^*_{avg}}{k^*_{ripple}P^*_{Cu}} \tag{33}$$

where x and y represent the stator and rotor pole arc angles, respectively; T^*_{avg}, k^*_{ripple}, and P^*_{Cu} are the normalized average torque, torque ripple coefficient, and copper loss, respectively.

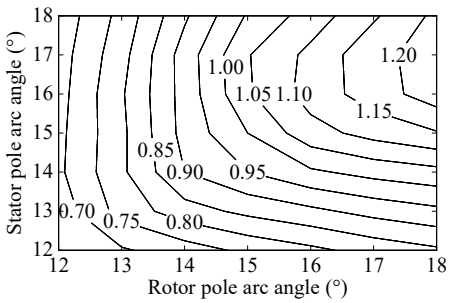

Fig. 14. Contour plot of the objective function.

Through the response surface method (RSM), the objective function is expressed as

$$F(x,y)=\frac{A_0+A_1x+A_2y+A_3y^2+A_4xy}{1+B_1x+B_2y+B_3x^2+B_4y^2+B_5xy} \tag{34}$$

where A_0=0.74565, A_1=-0.00338, A_2=-0.10514, A_3=0.00307, A_4=0.00135, B_1=0.0089, B_2=-0.13783, B_3=4.71197×10^{-4},

2332-7782 (c) 2020 IEEE. Personal use is permitted, but republication/redistribution requires IEEE permission. See http://www.ieee.org/publications_standards/publications/rights/index.html for more information.
Authorized licensed use limited to: Auckland University of Technology. Downloaded on December 19,2020 at 19:54:57 UTC from IEEE Xplore. Restrictions apply.

This article has been accepted for publication in a future issue of this journal, but has not been fully edited. Content may change prior to final publication. Citation information: DOI 10.1109/TTE.2020.3033668, IEEE Transactions on Transportation Electrification

B_4=0.00514, B_5=-9.63542×10^{-4}.

Bellow the base speed, the operation of SRMs is usually fed by the hysteresis current converter. The amplitudes of phase currents are limited. However, the phase inductance near unaligned rotor position has significant effect on the speed range above the base speed. This is due to the limited DC-link voltage. The optimization work should be subject to the current tracking capability [35].

At different configurations of the stator and rotor pole arc angles, the phase-current uprising angle (θ_{up}) before the current reaches the chopping level (i_{ref}) can be obtained by (35), where R_s is the phase resistance. In (35), assumption is made that the phase inductance is maintained at its minimum level before the stator pole starts to overlap the rotor pole. The calculated θ_{up} is shown in Fig. 15(a). To ensure the field-weakening capability above the base speed, the firing angle should not be ahead of the unaligned rotor position in the optimization. The half of the period of the minimum phase inductance (θ_{pr}) is defined by (36). The effect of the stator and rotor pole arc angles on θ_{pr} is shown in Fig. 15(b). It is indicated in Fig. 15 that, with the increase of either the stator pole arc angle or the rotor pole arc angle, θ_{up} increases, while θ_{pr} decreases.

$$\theta_{up} = -\frac{6nL_u}{R_s}\ln\left(1-\frac{i_{ref}R_s}{V_{DC}}\right) \tag{35}$$

$$\theta_{pr} = \frac{\tau_r - \tau_s\alpha_s - \tau_r\alpha_r}{2} \tag{36}$$

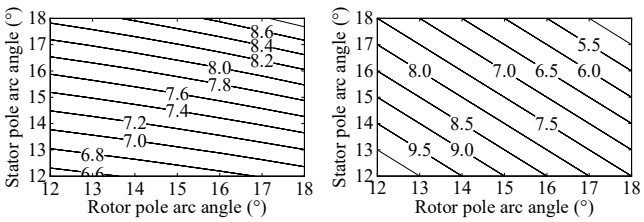

(a) (b)

Fig. 15. Influence of stator and rotor pole arc angles on (a) phase-current uprising angle and (b) half of the period of minimum phase inductance.

To ensure the current tracking capability below the base speed, θ_{up} should not be larger than θ_{pr}. Besides, the stator pole arc angle is generally smaller than the rotor one. The constraints of the optimization are as follows:

$$\begin{cases} G = \theta_{up} - \theta_{pr} \le 0 \\ G' = \tau_s\alpha_s - \tau_r\alpha_r \le 0 \end{cases} \tag{37}$$

where

$$\theta_{up} = 5.6659 - 0.16081x + 0.01854y + 0.00416x^2 + 0.00573y^2 + 0.00799xy,$$

$$\theta_{pr} = 22.5 - 0.5x - 0.5y - 2.36738\cdot10^{-18}x^2 - 4.08211\cdot10^{-17}y^2 - 4.0371\cdot10^{-17}xy.$$

Through the optimization to obtain the maximum value of the objective function (34) under the constraints (37), the optimal stator and rotor pole arc angles are both nearly 15°, which are just the default values in the initial design.

E. Analysis of Skewed Rotor Segment

For further improvement of the motor performance, the skewed rotor segment is investigated. The skewed rotor segment profile is shown in Fig. 16. In Fig. 16, the edges at the sliding-in and sliding-out sides are skewed in the opposite direction, and the skewed angle is denoted by θ.

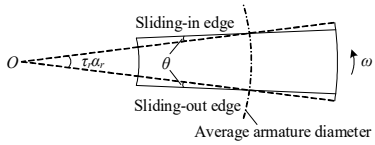

Fig. 16. Geometry of the skewed rotor segment.

As stated in the foregoing part, the current tracking capability is related with the unaligned phase inductance. To maintain the unaligned phase inductance, the two edges of the rotor segment are skewed with fixed rotor pole arc angle at the average armature diameter shown in Fig. 16. The average armature diameter is at the middle of the excitation pole.

As shown in Fig. 9, the total reluctance of single excitation pole is

$$R_a = 2R_g + \frac{2R_{go}R_{gi}}{R_{go}+R_{gi}} = \frac{2\delta}{\mu_0 S_m} + \frac{2\delta}{\mu_0\left(S_o+S_i\right)} \tag{38}$$

where $S_m = \frac{\pi D_{av}\alpha_s l_{ef}}{Z_s}$, $S_o = \frac{\pi D_{avo}\alpha_r l_{efo}}{Z_r}$, and $S_i = \frac{\pi D_{avi}\alpha_r l_{efi}}{Z_r}$ are the cross-sectional areas of the main flux flowing through the air gaps at the excitation pole and the outer and inner flux-conductive rings, respectively.

It is indicated that R_a is reversely proportional to (S_o+S_i). From (21) and (23), it is indicated that the average torque is related with the aligned phase inductance. For approximately constant aligned phase inductance, the study of skewed rotor segment is carried out under the constraint of S_o=S_i=0.5S_m along with the fixed outer diameter and volume of the motor.

The influences of the skewed angle on the motor performance are shown in Fig. 17.

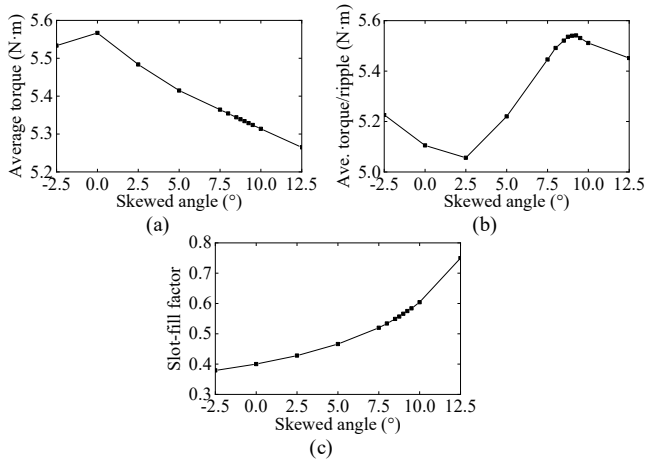

(a) (b) (c)

Fig. 17. Effect of skewed angle on (a) average torque, (b) average torque per unit ripple, and (c) slot-fill factor of the slot at the outer side of the excitation pole.

As shown in Fig. 17(a), the average torque decreases monotonously with the increase of the skewed angle. However, the average torque per unit ripple reaches its maximum value at 8.75° as shown in Fig. 17(b). Hence, the optimal skewed angle

2332-7782 (c) 2020 IEEE. Personal use is permitted, but republication/redistribution requires IEEE permission. See http://www.ieee.org/publications_standards/publications/rights/index.html for more information.
Authorized licensed use limited to: Auckland University of Technology. Downloaded on December 19,2020 at 19:54:57 UTC from IEEE Xplore. Restrictions apply.

This article has been accepted for publication in a future issue of this journal, but has not been fully edited. Content may change prior to final publication. Citation information: DOI 10.1109/TTE.2020.3033668, IEEE Transactions on Transportation Electrification

is 8.75°. The average torque decreases by 4%, while the torque ripple coefficient decreases by about 12%.

In addition, due to the constraint of the fixed outer diameter and volume, the slot-fill factor of the slot at the outer side of the excitation pole increases monotonously with the increase of the skewed angle as shown in Fig. 17(c). When the skewed angle increases to 8.75°, the slot-fill factor increases from 0.4 to 0.557, which is acceptable for the motor assembly.

IV. Simulation Results and Comparisons

In this section, 3D FEM is utilized for the verification of the performance of ADS-SRM, and then, the comparison of the performance between ADS-SRM and the existing topology is implemented.

The dynamic performance of the motor is obtained by the motion-coupled analysis. The motor is driven by the asymmetric half-bridge converter. Fig. 18 shows the simulated three-phase currents and torque output at the rated speed. The simulated performance parameters at the rated condition are summarized in Table IV.

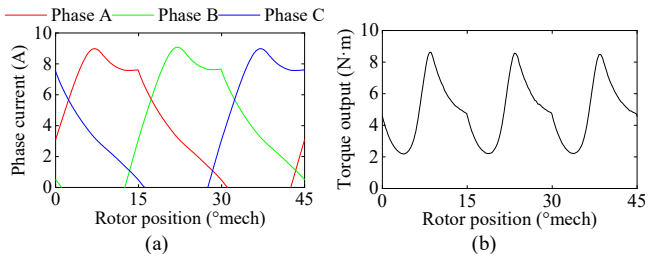

Fig. 18. Simulated (a) three-phase currents and (b) torque output at the rated condition.

TABLE IV
Simulated Performance Parameters of Three-Phase 12/8 ADS-SRM at Rated Condition

Parameter	Value
Average torque (N·m)	4.87
Current density (A/mm^2)	5.25
Copper loss (W)	167.94
Iron loss (W)	63.17
Efficiency (%)	81.5

Since the magnetic flux traveling in the excitation pole of ADS-SRM is straightforward from one motor side to the other and the stator yoke is cancelled, the existing YASA topology is chosen for comparison [36], [37]. The stator/rotor pole configuration and the coil arrangement of YASA-AFSRM and ADS-SRM are depicted in Fig. 19. Both the motors have 12 stator poles and 8 rotor poles/segments. For fair comparisons, the two motors are designed at the same outer diameter, volume, and ratings.

The torque production capabilities of the two motors are examined at the same excitations through 3D FEM. Fig. 20 shows their flux linkage-current diagrams. It is observed that the torque produced by YASA-AFSRM are slightly higher than that by ADS-SRM at low current levels since the area enclosed by the flux linkage-current loci between the unaligned and aligned rotor positions denotes the conversion from the electrical energy to the mechanical energy. However, at high current levels, the torque produced by the latter is significantly higher than that by the former. It is further verified by their static-torque characteristics shown in Fig. 21. In Fig. 21, the torque profiles in red denote the phase excitation at the rated condition (8A). In this condition, the average torques produced by the two motors are identical. Fig. 22 shows their average torques at various current densities and power losses at 200 r/min. It is indicated that the torque production capability is significantly improved in ADS-SRM.

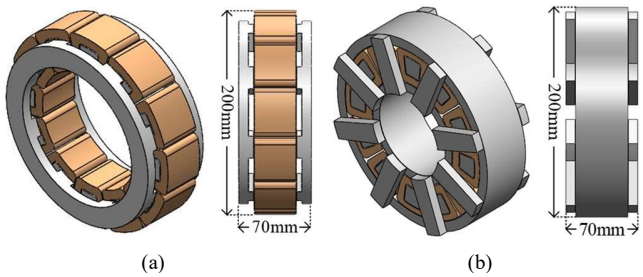

Fig. 19. Detailed motor geometry of (a) YASA-AFSRM and (b) the discussed ADS-SRM.

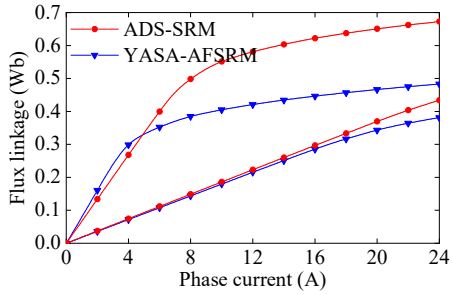

Fig. 20. Flux linkage loci with increasing current levels.

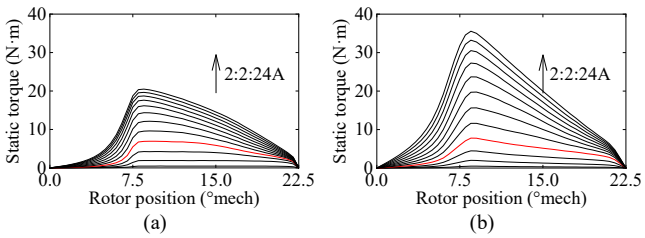

Fig. 21. Static-torque characteristics of (a) YASA-AFSRM and (b) ADS-SRM.

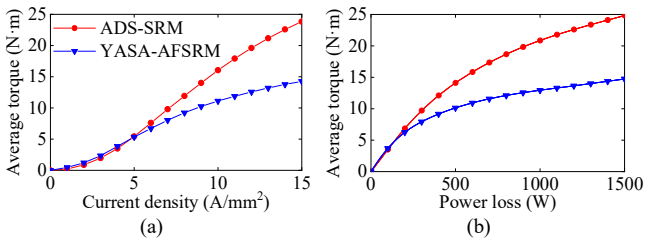

Fig. 22. Torque-production capabilities versus (a) current density and (b) power loss at 200 r/min.

V. Manufacturing Details

Fig. 23 shows the cross-sectional view of the assembly drawing of ADS-SRM, and the prototype is shown in Fig. 24. All the stator components are manufactured by spirally wound laminated steel (50DW470), and are held together by filling epoxy resin. The rotor consists of two groups of rotor segments, which are inserted in the nonmagnetic rotor brackets (Aluminum alloy) at each rotor side. The two rotor sides face

2332-7782 (c) 2020 IEEE. Personal use is permitted, but republication/redistribution requires IEEE permission. See http://www.ieee.org/publications_standards/publications/rights/index.html for more information.
Authorized licensed use limited to: Auckland University of Technology. Downloaded on December 19,2020 at 19:54:57 UTC from IEEE Xplore. Restrictions apply.

This article has been accepted for publication in a future issue of this journal, but has not been fully edited. Content may change prior to final publication. Citation information: DOI 10.1109/TTE.2020.3033668, IEEE Transactions on Transportation Electrification

the internal stator and are in alignment. The concentrated windings are not visible in the photograph due to the epoxy potting. The opposite external rotor sides are connected together through the rotor frame (Aluminum alloy).

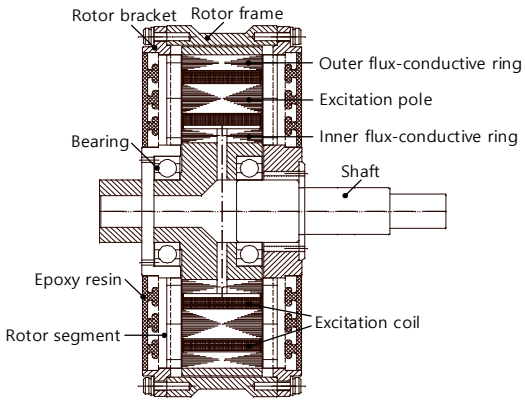

Fig. 23. Cross-sectional view of the assembly drawing.

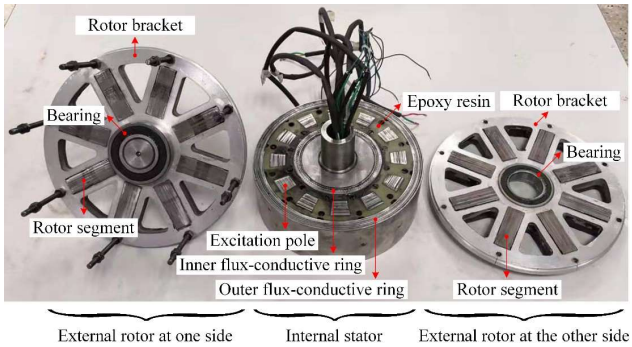

Fig. 24. Prototype of the three-phase 12/8 ADS-SRM.

VI. Experimental Verification

Fig. 25 shows the experimental setup of ADS-SRM. The motor is coupled to a magnetic brake load through the torque transducer.

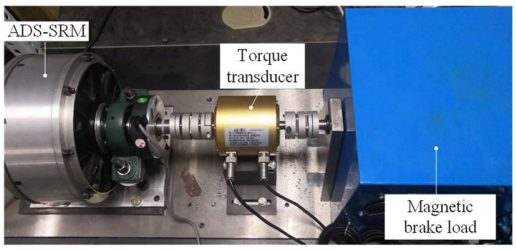

Fig. 25. Experimental setup.

As shown in (1) and (2), the magnetization characteristics are essential for the prediction of the torque production. The flux linkage-current diagram can be experimentally obtained by an indirect method when the rotor is locked at any specified position [38]. This method is based on the measured voltage and current of a phase, and then, (39) is applied to compute the flux linkages. Fig. 26 shows the measured voltages and currents at unaligned and aligned rotor positions, and the computed flux linkage-current diagram is presented in Fig. 27. It is observed that the discrepancies are significant at aligned position at high current levels. The main cause can be attributed to the uncertainties of the magnetic property of the core material. Besides, the dimensional discrepancy due to the manufacturing and assembly tolerance is not considered in FEM.

$$\psi(n)=\sum_{k=1}^{n} v(k)-Ri(k)T_s\big|_{\theta=const.} \tag{39}$$

where n, k, and T_s are the number of sampling point, the kth sampling point, and the sampling period, respectively.

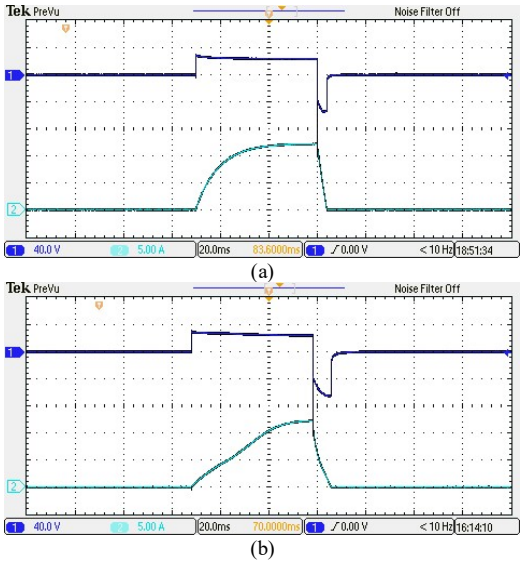

Fig. 26. Measured voltages and currents at (a) unaligned and (b) aligned rotor positions.

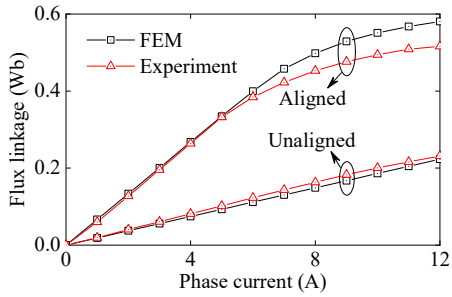

Fig. 27. Flux linkage-current diagram obtained from FEM and experiment.

The static torque measurements are conducted by injecting currents into the motor phase when the rotor is locked at different rotor positions. Fig. 28 shows the testing results.

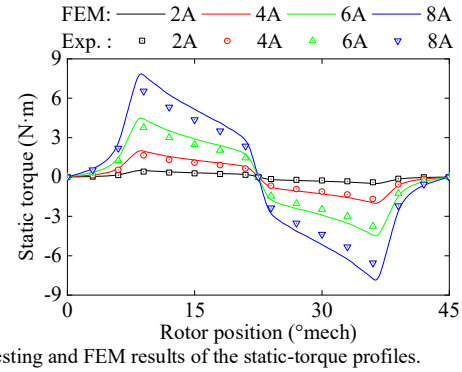

Fig. 28. Testing and FEM results of the static-torque profiles.

A closed-loop control is performed to test the dynamic performance of ADS-SRM. Fig. 29 shows the variation of the

2332-7782 (c) 2020 IEEE. Personal use is permitted, but republication/redistribution requires IEEE permission. See http://www.ieee.org/publications_standards/publications/rights/index.html for more information.
Authorized licensed use limited to: Auckland University of Technology. Downloaded on December 19,2020 at 19:54:57 UTC from IEEE Xplore. Restrictions apply.

This article has been accepted for publication in a future issue of this journal, but has not been fully edited. Content may change prior to final publication. Citation information: DOI 10.1109/TTE.2020.3033668, IEEE Transactions on Transportation Electrification

measured RMS values of the phase current with the rotor speed at different loads.

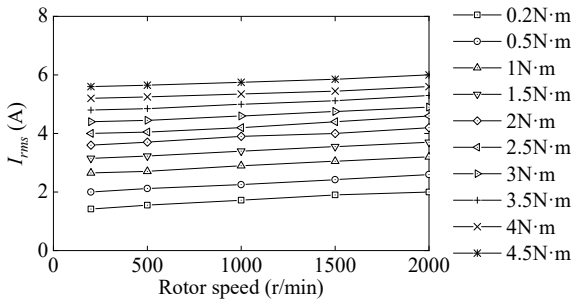

Fig. 29. Measured RMS values of phase current versus rotor speed at different loads.

VII. Conclusion

This paper has presented the design, optimization, fabrication details and experimental verification of a novel ADS-SRM. The operating principle is introduced and the stator/rotor pole combinations are analyzed. Based on the MEC models of ADS-SRM, the output equation and the winding design are derived considering the coefficients of phase inductance, fringing and leakage field. The 3D finite-element model is built, and the optimizations of main geometric parameters, which were determined empirically, are carried out. Furthermore, the investigation of skewed rotor segment is carried out. The average torque decreases by 4%, while the torque ripple coefficient decreases by about 12%. Moreover, through the motor performance comparisons with YASA-AFSRM, it is found that the torque production capability can be significantly improved in ADS-SRM. Finally, the prototype manufacturing is depicted in detail, and the experimental measurements validate the motor performances.

References

[1] R. Krishnan, "Switched reluctance motor drives: modeling, simulation, analysis, design and applications," Boca Raton, FL: CRC Press, Jun. 2001.

[2] D. Lee, T. H. Pham and J. Ahn, "Design and operation characteristics of four-two pole high-speed SRM for torque ripple reduction," IEEE Transactions on Industrial Electronics, vol. 60, no. 9, pp. 3637-3643, Sept. 2013.

[3] E. W. Fairall, B. Bilgin, and A. Emadi, "State-of-the-art high-speed switched reluctance machines," IEEE International Electric Machines and Drives Conference, Coeur d'Alene, ID, USA, pp. 1621-1627, may 2015.

[4] E. Bostanci, M. Moallem, A. Parsapour and B. Fahimi, "Opportunities and challenges of switched reluctance motor drives for electric propulsion: a comparative study," IEEE Transactions on Transportation Electrification, vol. 3, no. 1, pp. 58-75, Mar. 2017.

[5] C. Gan, J. Wu, Q. Sun, W. Kong, H. Li and Y. Hu, "A review on machine topologies and control techniques for low-noise switched reluctance motors in electric vehicle applications," IEEE Access, vol. 6, pp. 31430-31443, 2018.

[6] J. Lin, N. Schofield and A. Emadi, "External-rotor 6-10 switched reluctance motor for an electric bicycle," IEEE Transactions on Transportation Electrification, vol. 1, no. 4, pp. 348-356, Dec. 2015.

[7] B. Howey, B. Bilgin and A. Emadi, "Design of a mutually coupled external-rotor direct drive E-bike switched reluctance motor," IET Electrical Systems in Transportation, vol. 10, no. 1, pp. 89-95, 3 2020.

[8] S. Li, S. Zhang, T. G. Habetler and R. G. Harley, "Modeling, design optimization, and applications of switched reluctance machines—a review," IEEE Transactions on Industry Applications, vol. 55, no. 3, pp. 2660-2681, May-June 2019.

[9] R. Cao, E. Su and M. Lu, "Comparative study of permanent magnet assisted linear switched reluctance motor and linear flux switching permanent magnet motor for railway transportation," IEEE Transactions on Applied Superconductivity, vol. 30, no. 4, pp. 1-5, June 2020.

[10] I. Boldea, L. N. Tutelea, L. Parsa and D. Dorrell, "Automotive electric propulsion systems with reduced or no permanent magnets: an overview," IEEE Transactions on Industrial Electronics, vol. 61, no. 10, pp. 5696-5711, Oct. 2014.

[11] K. M. Rahman and S. E. Schulz, "Design of high-efficiency and high-torque-density switched reluctance motor for vehicle propulsion," IEEE Transactions on Industry Applications, vol. 38, no. 6, pp. 1500-1507, Nov.-Dec. 2002.

[12] S. Wang, Q. Zhan, Z. Ma and L. Zhou, "Implementation of a 50-kW four-phase switched reluctance motor drive system for hybrid electric vehicle," IEEE Transactions on Magnetics, vol. 41, no. 1, pp. 501-504, Jan. 2005.

[13] A. Chiba et al., "Torque density and efficiency improvements of a switched reluctance motor without rare-earth material for hybrid vehicles," IEEE Transactions on Industry Applications, vol. 47, no. 3, pp. 1240-1246, May-June 2011.

[14] K. Kiyota and A. Chiba, "Design of switched reluctance motor competitive to 60-kW IPMSM in third-generation hybrid electric vehicle," IEEE Transactions on Industry Applications, vol. 48, no. 6, pp. 2303-2309, Nov. 2012.

[15] J. W. Jiang, B. Bilgin and A. Emadi, "Three-phase 24/16 switched reluctance machine for a hybrid electric powertrain," IEEE Transactions on Transportation Electrification, vol. 3, no. 1, pp. 76-85, Mar. 2017.

[16] A. Cavagnino, M. Lazzari, F. Profumo and A. Tenconi, "A comparison between the axial flux and the radial flux structures for PM synchronous motors," IEEE Transactions on Industry Applications, vol. 38, no. 6, pp. 1517-1524, Nov.-Dec. 2002.

[17] H. Torkaman, A. Ghaheri and A. Keyhani, "Axial flux switched reluctance machines: a comprehensive review of design and topologies," IET Electric Power Applications, vol. 13, no. 3, pp. 310-321, 3 2019.

[18] T. J. Woolmer and M. D. McCulloch, "Analysis of the yokeless and segmented armature machine," 2007 IEEE International Electric Machines & Drives Conference, Antalya, 2007, pp. 704-708.

[19] B. Bilgin, A. Emadi and M. Krishnamurthy, "Design considerations for switched reluctance machines with a higher number of rotor poles," IEEE Transactions on Industrial Electronics, vol. 59, no. 10, pp. 3745-3756, Oct. 2012.

[20] B. Bilgin, A. Emadi and M. Krishnamurthy, "Comprehensive evaluation of the dynamic performance of a 6/10 SRM for traction application in PHEVs," IEEE Transactions on Industrial Electronics, vol. 60, no. 7, pp. 2564-2575, July 2013.

[21] R. Madhavan and B. G. Fernandes, "Performance improvement in the axial flux-segmented rotor-switched reluctance motor," IEEE Transactions on Energy Conversion, vol. 29, no. 3, pp. 641-651, Sept. 2014.

[22] B.C. Mecrow, J.W. Finch, E.A. El-Kharashi, A.G. Jack, "Switched reluctance motors with segmental rotors," IEE Proceedings-Electric Power Applications, vol. 149, no. 4, pp. 245-254, 2002.

[23] B. C. Mecrow, E. A. El-Kharashi, J. W. Finch and A. G. Jack, "Preliminary performance evaluation of switched reluctance motors with segmental rotors," IEEE Transactions on Energy Conversion, vol. 19, no. 4, pp. 679-686, Dec. 2004.

[24] R. Madhavan and B. G. Fernandes, "Axial flux segmented SRM with a higher number of rotor segments for electric vehicles," IEEE Transactions on Energy Conversion, vol. 28, no. 1, pp. 203-213, March 2013.

[25] Pere Andrada, Balduí Blanqué, Eusebi Martínez, José Ignacio Perat, José Antonio Sánchez and Marcel Torrent, "Design of a novel modular axial-flux double rotor switched reluctance drive," Energies, vol. 13, issue 5, pp. 1-17, 2020.

[26] W. Sun, Q. Li, K. Liu and L. Li, "Design and analysis of a novel rotor-segmented axial-field switched reluctance machine," CES Transactions on Electrical Machines and Systems, vol. 1, no. 3, pp. 238-245, Sept. 2017.

[27] J. Lin, T. Lambert, Y. Yang, B. Bilgin, R. Lankin and A. Emadi, "A novel axial flux switched reluctance motor with multi-level air gap geometry," 2016 IEEE Electrical Power and Energy Conference (EPEC), Ottawa, ON, 2016, pp. 1-8.

[28] Y. Wang, Z. Q. Zhu, J. Feng, S. Guo, Y. F. Li and Y. Wang, "Investigation of unbalanced magnetic force in fractional-slot PM machines having an odd number of stator slots," IEEE Transactions on Energy Conversion, doi: 10.1109/TEC.2020.2995803.

2332-7782 (c) 2020 IEEE. Personal use is permitted, but republication/redistribution requires IEEE permission. See http://www.ieee.org/publications_standards/publications/rights/index.html for more information.
Authorized licensed use limited to: Auckland University of Technology. Downloaded on December 19,2020 at 19:54:57 UTC from IEEE Xplore. Restrictions apply.

This article has been accepted for publication in a future issue of this journal, but has not been fully edited. Content may change prior to final publication. Citation information: DOI 10.1109/TTE.2020.3033668, IEEE Transactions on Transportation Electrification

[29] V. R and B. G. Fernandes, "Design methodology for high-performance segmented rotor switched reluctance motors," IEEE Transactions on Energy Conversion, vol. 30, no. 1, pp. 11-21, March 2015.
[30] R. Krishnan, M. Abouzeid and X. Mang, "A design procedure for axial field switched reluctance motors," Conference Record of the 1990 IEEE Industry Applications Society Annual Meeting, Seattle, WA, USA, 1990, pp. 241-246 vol.1.
[31] J. F. Gieras, "Electrical machines: fundamentals of electromechanical energy conversion," Boca Raton FL USA: CRC Press, 2016.
[32] Y. Yang, N. Schofield and A. Emadi, "Double-rotor switched reluctance machine (DRSRM)," IEEE Transactions on Energy Conversion, vol. 30, no. 2, pp. 671-680, June 2015.
[33] R. Arumugam, J. F. Lindsay and R. Krishnan, "Sensitivity of pole arc/pole pitch ratio on switched reluctance motor performance," Conference Record of the 1988 IEEE Industry Applications Society Annual Meeting, Pittsburgh, PA, USA, 1988, pp. 50-54 vol.1.
[34] J. G. Amoros and P. Andrada, "Sensitivity analysis of geometrical parameters on a double-sided linear switched reluctance motor," IEEE Transactions on Industrial Electronics, vol. 57, no. 1, pp. 311-319, Jan. 2010.
[35] A. D. Callegaro, B. Bilgin and A. Emadi, "Radial force shaping for acoustic noise reduction in switched reluctance machines," IEEE Transactions on Power Electronics, vol. 34, no. 10, pp. 9866-9878, Oct. 2019.
[36] S. Murakami, H. Goto and O. Ichinokura, "A study about optimum stator pole design of axial-gap switched reluctance motor," 2014 International Conference on Electrical Machines (ICEM), Berlin, 2014, pp. 975-980.
[37] H. Goto, T. Shibamoto, K. Nakamura and O. Ichinokura, "Development of high torque density axial-gap switched reluctance motor for in-wheel direct-drive EV," 2013 15th European Conference on Power Electronics and Applications (EPE), Lille, 2013, pp. 1-7.
[38] S. Song, M. Zhang and L. Ge, "A new fast method for obtaining flux-linkage characteristics of SRM," IEEE Transactions on Industrial Electronics, vol. 62, no. 7, pp. 4105-4117, July 2015.

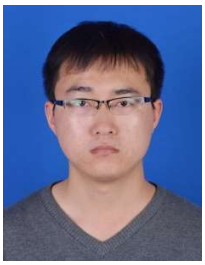

Wei Sun was born in Jiangsu Province, China. He received the B.S. degree in electrical engineering from Nanjing University of Science and Technology (NJUST), Nanjing, China, in 2014.

He is currently pursuing the Ph.D. degree in the School of Automation, NJUST, Nanjing, China. His main research interest focuses on electric motor design and control.

Qiang Li was born in Jiangsu Province, China. He received the B.S. degree from Harbin Institute of Technology (HIT), Harbin, China, in 1992, and the Ph.D. degree in electrical engineering from Southeast University, Nanjing, China, in 2005.

In 2005, he joined the Department of Electrical Engineering, School of Automation, Nanjing University of Science and Technology (NJUST), where he has been engaged in teaching and research in the field of electrical engineering. His main research interests include electric motor design, motor control, switching mode power supply, and embedded systems.

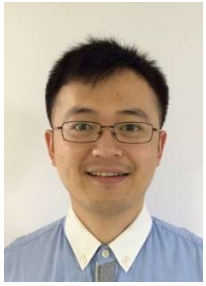

Le Sun (IEEE S'15–M'17) received the B.S. and M.S. degrees from Nanjing University of Aeronautics and Astronautics, Nanjing, China, in 2009 and 2012, respectively, and the Ph.D. degree in electrical engineering from the School of Electrical Engineering, Southeast University, Nanjing, China, in 2016.

He is now working as an associate professor in the department of electrical engineering, Nanjing University of Science and Technology (NJUST), Nanjing, China. From 2012 to 2013, he was a R&D Engineer with the United Automotive Electronic Systems Company, Ltd., Shanghai. From 2016 to 2018, he was working with the McMaster Automotive Resource Centre, McMaster University, where he was leading a research team of the motor control technologies. His research interest includes analysis, design, and control of permanent-magnet motors and power management techniques for electric vehicle (EV) and hybrid EV applications.

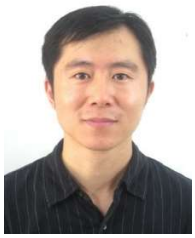

Lei Li received the B.S. degree in electrical technology from Shandong University of Science and Technology, Jinan, China, and the Ph.D. degree in power electronics and power drive from Nanjing University of Aeronautics and Astronautics, Nanjing, China, in 1997 and 2004, respectively.

In 2005, he joined the Faculty of Electrical Engineering, School of Automation, Nanjing University of Science and Technology, where he has been engaged in teaching and research in the field of power electronics and power drive. His main research interests include switching mode power supply, multilevel converters and control technique.

2332-7782 (c) 2020 IEEE. Personal use is permitted, but republication/redistribution requires IEEE permission. See http://www.ieee.org/publications_standards/publications/rights/index.html for more information.
Authorized licensed use limited to: Auckland University of Technology. Downloaded on December 19,2020 at 19:54:57 UTC from IEEE Xplore. Restrictions apply.